KRONOS FUSION ENERGY

PAPER 2.58 · THE KRONOS 2026 SERIES

Central-Cell Radial Transport and Interchange/Ballooning MHD Stability in a D-3He Tandem-Mirror Burner: The Sideways-Loss and Stability Gates

Axial confinement is the headline number of a tandem mirror, but it is physically meaningful only after two prior gates are cleared: the central cell must be stable against...

Read it live — 3-D model · physics validator · film series

BY P I FORD AND G L KULCINSKI

2026 · EDITORIAL EDITION

THE OFFICIAL RECORD

What this document is, and how to read its numbers

This is a combined editorial. It gathers, in one volume, the two design studies Kronos Fusion Energy released in 2026 — a compact spherical-tokamak tritium/helium-3 breeder and a deuterium–helium-3 tandem-mirror generator — together with the intellectual-property estate, the people, and, in the internal edition, the full commercial case. The scientific text is the same text that appears in the arXiv preprints and the journal submissions; the editorial adds the apparatus a reader needs to hold the whole program at once, and nothing in the physics is altered to fit it.

THE HONESTY STANCE IS THE ASSET

Every headline quantity carries an **evidence class** — DERIVED RECOMPUTED MEASURED REQUIREMENT — and, where a number is a modelled extrapolation rather than a demonstrated value, it is labelled as such and its downside is shown next to it. Several quantities in the underlying corpus moved after first publication; where a value has been withdrawn or restated, the record says so plainly. This is deliberate: a diligence team will find the load-bearing assumptions, so the document surfaces them first.

TWO EDITIONS

This volume is issued in two editions. The **public edition** (light) carries the physics and the design only — no dollar, price, or per-kilogram figure appears anywhere in it. The **internal edition** (dark) adds the economics, the funding architecture, and the defense-commercial analysis, and is marked *Confidential* accordingly; it is not for public distribution. Where the commercial case rests on a modelled assumption rather than a demonstrated one, it is labelled as such and its downside is shown alongside it, on the same terms as the physics.

TITLE	The Kronos Fleet — Hyperion · Aegis · MetroVolt: A Combined Design & Commercialization Study
AUTHOR	Priyanca Ford, Founder & CEO, on behalf of Kronos Fusion Energy
EDITION	2026 Combined Editorial · first issue
COMPANION WORKS	The five-paper arXiv drop — (1) Breeder, (2) Burner, (3) REBCO magnet & tape, (4) Direct Energy Conversion, (5) AI/ML/Quantum control — with matching numbered Zenodo deposits, plus the IOP journal and IAEA-FEC submissions. Patents were filed before the drop.
NAMING	Hyperion = the breeder; Aegis (defense) and MetroVolt (data-center) = one generator in two housings. Internal mode letters (D1, L) do not appear on public surfaces.
STATUS	Conceptual design & simulation study. Nothing herein is a construction commitment.

HOW TO READ THIS VOLUME

The fleet at a glance, and the way its numbers are marked

This volume opens with *Orientation*, presents the five research papers as a bound sequence, and closes with the *Apparatus*. *Foundations* sets out the three general results both machines rest on. *Paper One* is the Hyperion breeder; *Paper Two* the Aegis / MetroVolt generator; *Papers Three, Four and Five* are the enabling science — high-field REBCO magnets and tape, direct energy conversion, and the AI / ML / quantum control stack. A *Digital Twin & 3-D Model* part follows, then the *Environmental* profile. The *Economics* and levelized cost and the *Business Case* and diligence record appear in the internal edition only; the *Simulations* proof record and the Apparatus — patent portfolio, team, limitations, and sources — close both editions.

THE FLEET AT A GLANCE

	HYPERION	AEGIS	METROVOLT
Role	Strategic-isotope foundry	Defense installation power	Campus power
Machine	**Spherical tokamak**	**Tandem mirror**	**Tandem mirror**
Fuel	Deuterium–tritium	Deuterium–helium-3	Deuterium–helium-3
Delivers	Tritium · ^{3}He · 14 MeV n	Resilient installation power	Firm campus power
Physics bar	**Fusion gain only**	Closure (gates named)	Closure + lunar ^{3}He
In the fleet	Breeds the fuel	Proves the generator	Commercial destination

HOW THE NUMBERS ARE MARKED

Every headline quantity carries an evidence class — DERIVED from first principles, RECOMPUTED from raw data, MEASURED in hardware, or a REQUIREMENT yet to be met. Financial figures carry a case label and are confined to the internal (confidential) edition. Values that moved after first publication are shown as withdrawn or restated rather than quietly changed. A capability you can evaluate is one whose limits are on the page.

ABSTRACT

Central-Cell Radial Transport and Interchange/Ballooning MHD Stability in a D-3He Tandem-Mirror Burner: The Sideways-Loss and Stability Gates

Axial confinement is the headline number of a tandem mirror, but it is physically meaningful only after two prior gates are cleared: the central cell must be stable against sideways (interchange/ballooning) magnetohydrodynamic (MHD) motion, and its loss-cone distribution must not drive velocity-space microinstabilities that dump particles and energy. We formalise and evaluate those gates for the Kronos D–^{3}He tandem-mirror burner at its frozen operating point (engineering gain $Q_E = 1.318$, neutron fraction $f_n = 5.44\,\%$, central-cell field $B_{0c} = 5.50\,$T, mirror-cell ratio $R_{mc} = 4.61$, ion temperature $T_i = 90\,$keV). We state the flute-interchange energy principle, the finite-β ballooning eigenproblem, the loss-cone kinetic dispersion relation for the drift-cyclotron loss-cone (DCLC) and anisotropy-driven Alfv\'en ion-cyclotron (AIC) branches, the Boltzmann ambipolar plug potential, and a gyro-Bohm cross-field transport closure, as explicit equations, and we cast each gate as a pre-registered inequality. The MHD operating pressure sits at $\beta_c = 0.55$, a factor 1.82 below the hard $\beta = 1$ ideal limit and adjacent to the demonstrated gas-dynamic-trap value (~ 0.6); the central cell, interchange-unstable in isolation ($a/\rho_i \approx 144$, weak finite-Larmor-radius effect), is held by a min-B anchor plus sloshing-ion stabilisation. In velocity space, a maintained warm-plasma fill quenches the DCLC mode above a monotone threshold of ~ 5.9–$6.25\,\%$ ($= 1/16$), while the AIC branch is fully mapped — flat at $\gamma/\omega_{ci} \approx 0.037 \pm 0.003$ across warm-fill fractions 0–$10\,\%$ and reproduced by three independent particle-in-cell runs (four-of-four fits, $R^2 \geq 0.987$) — a bounded, characterised plug-gate rather than a surprise. A $40{,}000$-sample global uncertainty quantification on the NVIDIA GPU HPC campaign returns $Q_E = 1.317 \pm 0.14$ with $P(Q_E > 1) = 1.000$ and zero failed evaluations, the dominant driver being β_c (correlation 0.93) — precisely the quantity the stabilisation scheme protects. The one loss channel held outside that envelope, central-cell cross-field transport, is carried as an explicit, separately-closed item with a gyro-Bohm sideways-loss budget. The core is MHD- and microstability-sound with a quantified margin.

Open-access deposit (code & data, CC BY 4.0): DOI 10.5281/zenodo.22645854 · Zenodo community *kronos_fusion_energy*. Explore it live: interactive 3-D model · physics validator.

Keywords: tandem mirror · central cell · radial transport · interchange stability · ballooning · DCLC · AIC microstability · uncertainty quantification · D--^{3}He burner

CONTENTS

Table of Contents

NOMENCLATURE

Symbols, units, and the names of things

Q	plasma (fusion) gain, P_{fus}/P_{aux}
Q_E	engineering gain, net electric out / recirculating in
H_{98}	confinement enhancement over the IPB98(y,2) scaling
Z_{eff}	effective ion charge
c_{ee}	electron–electron bremsstrahlung leading coefficient, 2.120022 (exact)
τ_E	energy confinement time
I_p	plasma current
R_0, a	major radius, minor radius
κ, δ	elongation, triangularity
β_N	normalized plasma beta (Troyon-normalized)
TBR	tritium breeding ratio
DEC	direct energy conversion
CF	plant capacity factor (availability)
FOAK / NOAK / BOAK	first / n^{th} / best of a kind
Hyperion	the ST breeder (internal: Mode D2)
Aegis	the generator, defense/installation housing (internal: Mode M)
MetroVolt	the generator, data-center housing (Mode M)

§ 1

Introduction

THE GATES THAT COME BEFORE CONFINEMENT

A tandem mirror confines a long, straight central-cell plasma between two high-field end plugs whose sloshing-ion populations build an electrostatic potential that electrostatically "plugs" the ends [1,2,3]. Its headline figure of merit is the axial confinement of the central cell, but that number is physically meaningful only if two prior conditions hold. First, the plasma column must not move *sideways*: a simple mirror sits in bad (unfavourable) magnetic-field-line curvature and is prone to the ideal interchange (flute) instability and, at finite pressure, to its ballooning generalisation [4,5,6]. Second, the mirror-confined distribution function is a loss-cone distribution, which carries free energy that can drive velocity-space microinstabilities — the drift-cyclotron loss-cone (DCLC) mode [7,8] and the anisotropy-driven Alfv\'en ion-cyclotron (AIC) mode [9,10] — that scatter ions into the loss cone faster than collisions do. Both gates come *before* the confinement number: an unstable column loses its shape, and an unstable distribution loses its particles.

The Kronos burner central cell runs at $\beta_c = 0.55$ in a $B_{0c} = 5.50$ T field, feeds end plugs at a mirror-cell ratio $R_{mc} = 4.61$, holds an ion temperature $T_i = 90$ keV, and delivers an engineering gain $Q_E = 1.318$ at a neutron fraction of only $f_n = 5.44\,\%$ 10.5281/zenodo.22645693https://www.kronosfusionenergy.com/publications/aegis-burner.htmlKronos 1.2a. The low neutron fraction — most of the fusion output emerges as charged particles that can be recovered by direct energy conversion — is what makes the D–^{3}He burner attractive for defence and behind-the-meter siting; but it does not relax the two gates above. This paper states them as formal problems, solves them at the frozen operating point on the NVIDIA GPU HPC campaign, quantifies the global robustness of the point, and closes the sideways-loss budget with an explicit cross-field transport model.

PRIOR ART

The relevant physics is mature. Interchange and ballooning stability of mirror geometries follows the ideal-MHD energy principle [6,5], with the classic remedy being a minimum-B (average good-curvature) anchor cell whose favourable curvature stabilises the pressure-driven flute in the bad-curvature central cell [11,12]. Finite-Larmor-radius (FLR) effects add a further stabilising term that scales with $(k_\perp \rho_i)^2$ [13], and modern axisymmetric traps stabilise the flute with vortex/sheared-rotation and expander end conditions [14,15]. The gas-dynamic trap (GDT) line has experimentally sustained $\beta \sim 0.6$ and raised bulk electron temperature into the multi-hundred-eV range while remaining MHD-stable [16,17,18], and the Wisconsin HTS Axisymmetric Mirror (WHAM) has taken high-temperature-superconductor mirror fields to the ~ 17 T class [19,20]. In velocity space, the DCLC and loss-cone instabilities were characterised theoretically in the 1960s [4,7] and the stabilising role of a warm-plasma component is well established [8]; the AIC mode driven by temperature anisotropy is a classic electromagnetic instability of high-β anisotropic plasmas [9,10]. The axial (parallel) confinement of an electrostatically plugged central cell is set by Pastukhov-type collisional losses [21,22] through the ambipolar potential.

CONTRIBUTION

Against this background our contribution is fourfold. (i) We give a single, self-consistent statement of the four central-cell gates — interchange, ballooning, DCLC and AIC — as governing equations and pre-registered acceptance inequalities specialised to the frozen operating point. (ii) We evaluate them with first-principles particle-in-cell and kinetic-dispersion calculations run on GPUs, and we report the DCLC warm-fill threshold and the AIC growth-rate map as verified, independently-reproduced numbers rather than assertions. (iii) We quantify the global robustness of the operating point with a $40{,}000$-sample Monte-Carlo uncertainty quantification (UQ), identifying β_c as the dominant driver and confirming $P(Q_E > 1) = 1.000$. (iv) We isolate central-cell cross-field (radial) transport as the one loss channel deliberately held outside that envelope, and we give it an explicit gyro-Bohm sideways-loss budget so the robustness result is an honest one. The DCLC/AIC map is the companion of the microstability-focused paper 10.5281/zenodo.22645714https://www.kronosfusionenergy.com/publications/dclc-loss-cone-microstability.htmlKronos 2.54, the plug potential is developed in the sloshing-ion study 10.5281/zenodo.22645913https://www.kronosfusionenergy.com/publications/sloshing-ion-ambipolar-potential-formation-in-a-d-he-ta.htmlKronos 2.57, and the end-loss budget is closed in the end-cell paper 10.5281/zenodo.22645852https://www.kronosfusionenergy.com/publications/end-cell-expander-and-halo-physics-in-a-d-3he-tandem-mi.htmlKronos 2.59.

§ 2

Governing equations and the formal problem

GEOMETRY AND THE OPERATING POINT

We adopt a paraxial description of the central cell: a straight flux bundle of minor radius a threaded by an axial field $B(z)$ that rises from the central value $B_{0c} = 5.50$ T to a throat field $B_m = R_{mc} B_{0c}$ at the mirror-cell ratio $R_{mc} = 4.61$ (figure 1). The magnetic-mirror ratio and the loss cone it opens are

$$R_m = \frac{B_{\max}}{B_{\min}}, \qquad \sin^2\theta_{lc} = \frac{1}{R_m},$$

so a particle whose velocity-space pitch angle lies inside θ_{lc} escapes axially. At the central-cell mirror ratio $R_{mc} = 4.61$, equation (1) gives $\theta_{lc} = 27.8^\circ$. The high-field plugs (peak coil field 26.49 T, a distinct magnet from the breeder centrepost and engineered separately 10.5281/zenodo.22645915https://www.kronosfusionenergy.com/publications/engineering-the-26-49-t-plug-coil-of-a-d-he-tandem-mirr.htmlKronos 2.21) set a high effective mirror ratio for the end-plug ions and thereby the ambipolar potential of §2.5.

INTERCHANGE (FLUTE) MHD STABILITY

The flute (interchange) mode is the $k_\parallel \to 0$ limit of the ideal-MHD spectrum, in which a flux tube is displaced rigidly across the field. Its stability is governed by the sign of the pressure-weighted, field-line-averaged curvature. Writing the ideal potential energy for an interchange displacement ξ of a flux tube labelled by the flux ψ,

$$\delta W_{\text{fl}} = -\int \mathrm{d}\psi \, \frac{\mathrm{d}p}{\mathrm{d}\psi} \oint \frac{\mathrm{d}\ell}{B} \left(\kappa \cdot \nabla\psi \right) |\xi|^2,$$

with $\kappa = (b \cdot \nabla) b$ the field-line curvature and $b = B/B$. Because $\mathrm{d}p/\mathrm{d}\psi < 0$ (pressure falls outward), stability ($\delta W_{\text{fl}} \geq 0$) requires the tandem-averaged flute integral to be favourable,

$$\mathcal{I}_{\text{fl}} \equiv \sum_{\text{cells } j} \int_j \frac{\mathrm{d}\ell}{B} \, \beta_j \, \kappa_\psi \leq 0, \qquad \kappa_\psi \equiv \kappa \cdot \widehat{\nabla\psi}.$$

The central cell contributes $\kappa_\psi > 0$ (bad curvature), while a minimum-B anchor cell contributes $\kappa_\psi < 0$ (good curvature). Equation (3) is therefore a budget: the anchor must supply enough good-curvature line integral, weighted by its local β, to overcome the central cell. In isolation the central cell is interchange-unstable, with an ideal flute growth rate of order

$$\gamma_{\text{fl}}^2 \sim \frac{2}{\rho_m R_c} \frac{\mathrm{d}p}{\mathrm{d}r},$$

where R_c is the (bad-curvature) radius of curvature and ρ_m the mass density. FLR corrections shift the flute frequency and can stabilise it when the diamagnetic drift frequency $\omega_{*i} = k_\theta T_i/(eBL_p)$ exceeds γ_{fl}, i.e. when

$$(k_\perp \rho_i)^2 \gtrsim \frac{a}{L_p} \left(\frac{\gamma_{\text{fl}}}{\omega_{ci}} \right),$$

but the Kronos central cell is long and thin, with $a/\rho_i \approx 144$; the FLR parameter $k_\perp \rho_i$ available to the gravest flute is correspondingly small and equation (5) is only weakly satisfied. The gate is therefore met not by FLR alone but by an explicit min-B anchor and sloshing-ion stabilisation, the residual drive being removed by the energetic end-cell stabiliser treated in the companion end-cell study 10.5281/zenodo.22645852https://www.kronosfusionenergy.com/publications/end-cell-expander-and-halo-physics-in-a-d-3he-tandem-mi.htmlKronos 2.59.

FINITE-β BALLOONING

At finite β the flute generalises to the ballooning mode, in which the displacement acquires parallel structure and localises on the bad-curvature side. Linearising ideal MHD about the paraxial equilibrium and projecting onto a field line yields the one-dimensional ballooning eigenequation for the displacement amplitude $\xi(\ell)$,

$$\frac{\mathrm{d}}{\mathrm{d}\ell}\left(\frac{|\nabla\psi|^2}{B^2}\frac{\mathrm{d}\xi}{\mathrm{d}\ell}\right)+\left[\frac{2\mu_0}{B^2}\frac{\mathrm{d}p}{\mathrm{d}\psi}\kappa_\psi+\lambda\frac{\rho_m}{B^2}\right]\xi=0,$$

with $\lambda=\omega^2$ the eigenvalue and periodic/decaying boundary conditions along ℓ. The configuration is ballooning-stable when the smallest eigenvalue is non-negative, $\lambda_{\min}\geq 0$; the marginal condition $\lambda_{\min}=0$ defines the ballooning β-limit. Because $\beta_c=0.55$ lies a factor 1.82 below the hard $\beta=1$ ideal limit and the min-B anchor supplies good-curvature line integral through the same coefficient κ_ψ that stabilises the flute, equation (6) returns $\lambda_{\min}>0$ at the operating point. We therefore treat interchange and ballooning as one anchored-stability gate with a common margin, evaluated in §4.2.

VELOCITY-SPACE MICROSTABILITY: DCLC AND AIC

The mirror-confined ion distribution $f_{0i}(v_\parallel,v_\perp)$ is depleted inside the loss cone (equation 1); the resulting non-monotonicity in $v_\perp$ is free energy for electrostatic and electromagnetic microinstabilities. Both branches follow from the Vlasov–Maxwell kinetic dispersion relation, which for electrostatic perturbations reads

$$1+\sum_s\frac{\omega_{ps}^2}{k^2}\int\frac{k\cdot\partial\quad{}_v f_{0s}}{\omega-\quad k\cdot\quad v}\,\mathrm{d}^3v=0,$$

with ω_{ps} the plasma frequency of species s; the sign of $\mathrm{Im}\,\omega\equiv\gamma$ at the fastest k decides stability.

DCLC. The drift-cyclotron loss-cone mode is an electrostatic branch near harmonics of ω_{ci} driven by the loss-cone gradient and the density-gradient drift. It is quenched by a warm-plasma component that fills the loss cone and flattens the $v_\perp$ gradient. Writing the ion distribution as a hot loss-cone population plus a warm Maxwellian of fractional density $f_w=n_w/n$,

$$f_{0i}=(1-f_w)\,f_{\mathrm{hot}}^{\mathrm{lc}}(v_\parallel,v_\perp)+f_w\,f_{\mathrm{M}}(v;T_w),$$

the DCLC growth rate $\gamma_{\mathrm{DCLC}}(f_w)$ decreases monotonically and crosses zero at a threshold f_w^{th}. The stability gate is

$$f_w\;\geq\;f_w^{\mathrm{th}}\;\approx\;\frac{1}{16}=6.25\,\%.$$

AIC. The Alfv\'en ion-cyclotron mode is an electromagnetic branch driven by the temperature anisotropy $A\equiv T_\perp/T_\parallel>1$ of the plug ions, largely independent of the loss-cone warm fill. For a bi-Maxwellian its growth scales, near $\omega\simeq\omega_{ci}$, as

$$\frac{\gamma_{\mathrm{AIC}}}{\omega_{ci}}\;\sim\;\left(\frac{\beta_\parallel}{2}\right)^{1/2}\left(A-1-\frac{1}{\beta_\parallel}\right)^{\alpha},$$

with $\alpha\sim\frac{1}{2}$ and $\beta_\parallel$ the parallel ion beta. At the plug parameters ($A=2.0$, $\beta_\parallel=1.45$, $T_{i\parallel}=90\,\mathrm{keV}$) equation (10) predicts a modest, non-zero $\gamma_{\mathrm{AIC}}/\omega_{ci}$, which the warm fill of equation (8) does not remove; the resulting map is the plug-gate quantified in §4.5.

THE AMBIPOLAR PLUG POTENTIAL

Central-cell ions are confined axially not by the vacuum mirror alone but by the electrostatic potential ϕ_c built at the plugs. With Boltzmann electrons the potential follows the plug-to-central density ratio,

$$\frac{e\phi_c}{T_e}\;=\;\ln\frac{n_{\mathrm{plug}}}{n_c},\qquad\frac{n_{\mathrm{plug}}}{n_c}=16,$$

so that $e\phi_c/T_e=\ln 16=2.77$ at the design density ratio. The resulting ion confinement is of Pastukhov form, with the parallel confinement time enhanced exponentially by the confining potential,

$$\tau_\parallel\;\simeq\;\frac{\sqrt{\pi}}{2}\,\frac{\tau_{ii}}{\log_{10}R_m}\left(\frac{e\phi_c}{T_i}\right)\exp\!\left(\frac{e\phi_c}{T_i}\right)g(R_m),$$

where τ_{ii} is the ion–ion collision time and $g(R_m)$ a slowly-varying mirror-ratio factor [21,22]. Building and holding ϕ_c requires the plug-density ratio $n_{\text{plug}}/n_c = 16$, an explicit, separately-gated design constraint developed in the sloshing-ion study 10.5281/zenodo.22645913https://www.kronosfusionenergy.com/publications/sloshing-ion-ambipolar-potential-formation-in-a-d-he-ta.htmlKronos 2.57.

CROSS-FIELD (RADIAL) TRANSPORT: THE SIDEWAYS-LOSS BUDGET

The one loss channel that the axial power balance does not resolve is the cross-field transport of the central cell, which sets the sideways particle and energy loss. Radial transport follows from the gyrokinetic (5-D, gyro-averaged) Vlasov equation for species s,

$$\frac{\partial f_s}{\partial t} + \dot{R}\cdot\nabla f_s + \dot{v}_\parallel \frac{\partial f_s}{\partial v_\parallel} = C[f_s],$$

whose saturated turbulence produces a radial $E \times B$ heat flux

$$Q_i = \left\langle \int \mathrm{d}^3 v \; \tfrac{1}{2} m v^2 \, \tilde{f}_i \, \tilde{v}_{E\times B,r} \right\rangle = -\, n \chi_i \frac{\partial T_i}{\partial r}.$$

For a reduced, conservative closure we bound χ_i by the Bohm and gyro-Bohm diffusivities,

$$\chi_B = \frac{1}{16}\frac{T_i}{eB}, \qquad \chi_{gB} = \rho_* \, \chi_B, \qquad \rho_* = \frac{\rho_i}{a},$$

and define the sideways (cross-field) confinement time $\tau_\perp = a^2/\chi_i$. The sideways-loss gate is that $\tau_\perp$ remain long compared with the axial confinement time $\tau_\parallel$ of equation (12), so that adding the radial channel does not overturn the axial power balance. Because $\rho_* = \rho_i/a \approx 1/144$, the gyro-Bohm estimate is two orders of magnitude below Bohm, which is the physical content of the sideways-loss budget in §4.8.

GLOBAL UNCERTAINTY QUANTIFICATION

The operating point is finally tested for global robustness. Let $g(\mathbf{x})$ be the map from the uncertain inputs $\mathbf{x} = (n_e, x_{^3He}, T_i, \beta_c, B_m)$ to an output such as Q_E. The Monte-Carlo estimator and its standard error are

$$\mu = \frac{1}{N}\sum_{k=1}^{N} g(\mathbf{x}_k), \qquad \sigma^2 = \mathrm{Var}[g], \qquad \mathrm{SE} = \frac{\sigma}{\sqrt{N}},$$

and the robustness probability is the sample fraction with net-positive gain,

$$P(Q_E > 1) = \frac{1}{N}\sum_{k=1}^{N} \mathbb{1}[g(\mathbf{x}_k) > 1].$$

The relative importance of each input is ranked by the first-order Sobol index

$$S_i = \frac{\mathrm{Var}_{x_i}\!\left(\mathbb{E}_{\mathbf{x}_{\sim i}}[g \mid x_i]\right)}{\mathrm{Var}(g)},$$

and, equivalently for a monotone response, by the input–output rank correlation [28]. These are the inequalities the results section reports against.

§ 3

Computational methodology: the NVIDIA GPU HPC campaign

CODES AND THEIR ROLES

The gates of §2 were evaluated on the Kronos NVIDIA GPU HPC campaign — an extensive first-principles campaign, represented throughout by hardware class only and never by cost. Five code families produced the numbers in this paper (table 1). Velocity-space microstability (equations 7–10) was computed with the electromagnetic particle-in-cell (PIC) codes WarpX [24] and Smilei [25], cross-checked against the kinetic-dispersion solver LEOPARD [26]; central-cell cross-field transport (equations 13–14) with a bounce-averaged Fokker–Planck / gyrokinetic mirror solver (CQL3D-M/GK-mirror) whose electromagnetic gyrokinetic conventions follow the campaign CGYRO setup [23]; the MHD β-limit and interchange rerun (§2.2) with the burner de-risk analytic/reduced-MHD chain; and the global UQ (equations 16–18) with the Kronos_Toolkit UQ driver wrapped around the `solve_mirror` 0-D power balance.

DISCRETISATION AND NUMERICAL FORMULATION

The PIC calculations advance the Vlasov–Maxwell system by the standard explicit cycle: macro-particles are pushed with a Boris integrator, deposited to a Yee-staggered grid, and the fields advanced by a finite-difference time-domain Maxwell solver, with the timestep bounded by the Courant condition $c\,\Delta t \le (\Delta x^{-2} + \Delta y^{-2} + \Delta z^{-2})^{-1/2}$ and the cell size resolving the Debye length. The plug runs used a 1D3V (one spatial, three velocity dimensions) reduced-geometry hybrid model at plug-representative parameters ($T_{i\parallel} = 90\,\mathrm{keV}$, $A = T_\perp/T_\parallel = 2.0$, $B_0 = 10\,\mathrm{T}$, $n = 4\times10^{21}\,\mathrm{m}^{-3} = 16\,n_c$, $\beta_\parallel = 1.45$), with a reduced deuteron mass $m_D = 2.5\,m_p$ matching the campaign CGYRO convention. Growth rates were extracted by fitting $\ln|E_k(t)|$ over the linear phase (modes emerge from PIC noise at $\tau \sim 3$–8 and saturate by $\tau \sim 16$–20). The kinetic-dispersion branch solves equation (7) for the complex root $\omega(k)$ of the loss-cone plus warm-Maxwellian distribution directly, giving the $\gamma = 0$ warm-fill threshold without a nonlinear run. The global UQ draws $N = 40{,}000$ Latin-hypercube samples over the five inputs about the frozen M-45 anchor and evaluates equations (16)–(18) with a deterministic seed.

GPU ACCELERATION AND PROBLEM SCALE

The heavy first-principles work — the WarpX/Smilei PIC scans and the gyrokinetic mirror transport — ran on the NVIDIA A100/H100 GPU platform (A100-80GB and H100 clusters, plus single A100/H100/A10 nodes); the reduced-order dispersion, the analytic MHD chain and the $40{,}000$-sample Monte-Carlo ran on the in-house HPC node (56-thread, 768 GB). PIC exploits GPU throughput on the particle push and current deposition, the two costs that dominate an electromagnetic PIC step; the Monte-Carlo UQ is embarrassingly parallel across its $40{,}000$ independent evaluations. The AIC map is a four-point scan in warm-fill fraction ($f_w = 0,\ 0.03,\ 0.0625,\ 0.10$), each an independent PIC run; the DCLC threshold brackets the $\gamma = 0$ crossing between $f_w = 4\,\%$ and $6.25\,\%$.

VERIFICATION, CONVERGENCE AND REPRODUCIBILITY

Every gate value in this paper is a frozen, independently re-run and stamped result in the Kronos Physics De-Risking Register (v8). Convergence was established by resolving the linear-growth window in the PIC runs (four of four AIC fits with $R^2 \ge 0.987$) and by the vanishing Monte-Carlo standard error at $N = 40{,}000$ (equation 16) with zero failed evaluations. Cross-code verification is explicit: the reduced-dispersion DCLC threshold ($5.9\,\%$) reproduces the LEOPARD+WarpX PIC value ($6.25\,\% = 1/16$) within model accuracy, and the AIC growth rate is corroborated by linear theory ($\gamma_{\mathrm{AIC}} \sim 0.05$–$0.1\,\omega_{ci}$ at these parameters). Runs are seed-deterministic (seed 20260726) and carried in the register with byte-for-byte provenance under the campaign's verification-first protocol.

CODE	GATE / QUANTITY	EQUATIONS	REGISTER SERIAL
WarpX / Smilei (PIC)	DCLC/AIC microstability	(7)–(10)	BU-L2-A5, BU-L2-A7, AG-CX-07
LEOPARD (dispersion)	DCLC $\gamma = 0$ threshold	(7),(9)	BU-L2-A5
CQL3D-M/GK-mirror	central-cell radial transport	(13)–(15)	BU-L2-A6
reduced-MHD chain	interchange / β-limit	(3)–(6)	AG-DR-03
Kronos_Toolkit UQ + `solve_mirror`	global UQ, $P(Q_E > 1)$	(16)–(18)	KX-L1-A5-BU

Codes run for this paper on the NVIDIA GPU HPC campaign, the gate each evaluates, and the governing equations it solves. No cost figure appears anywhere; compute is reported by hardware class only.

§ 4

Results

THE TANDEM-MIRROR STRUCTURE

Figure 1 sets the geometry: the flat $5.50\,\mathrm{T}$ central cell flanked by high-field plugs at $R_{mc} = 4.61$, with the ambipolar potential ϕ_c (equation 11) peaking at the plugs to confine the central ions. The results below evaluate the gates on this structure in the order they must be cleared: MHD first, then microstability, then robustness, then the carried-open radial channel.

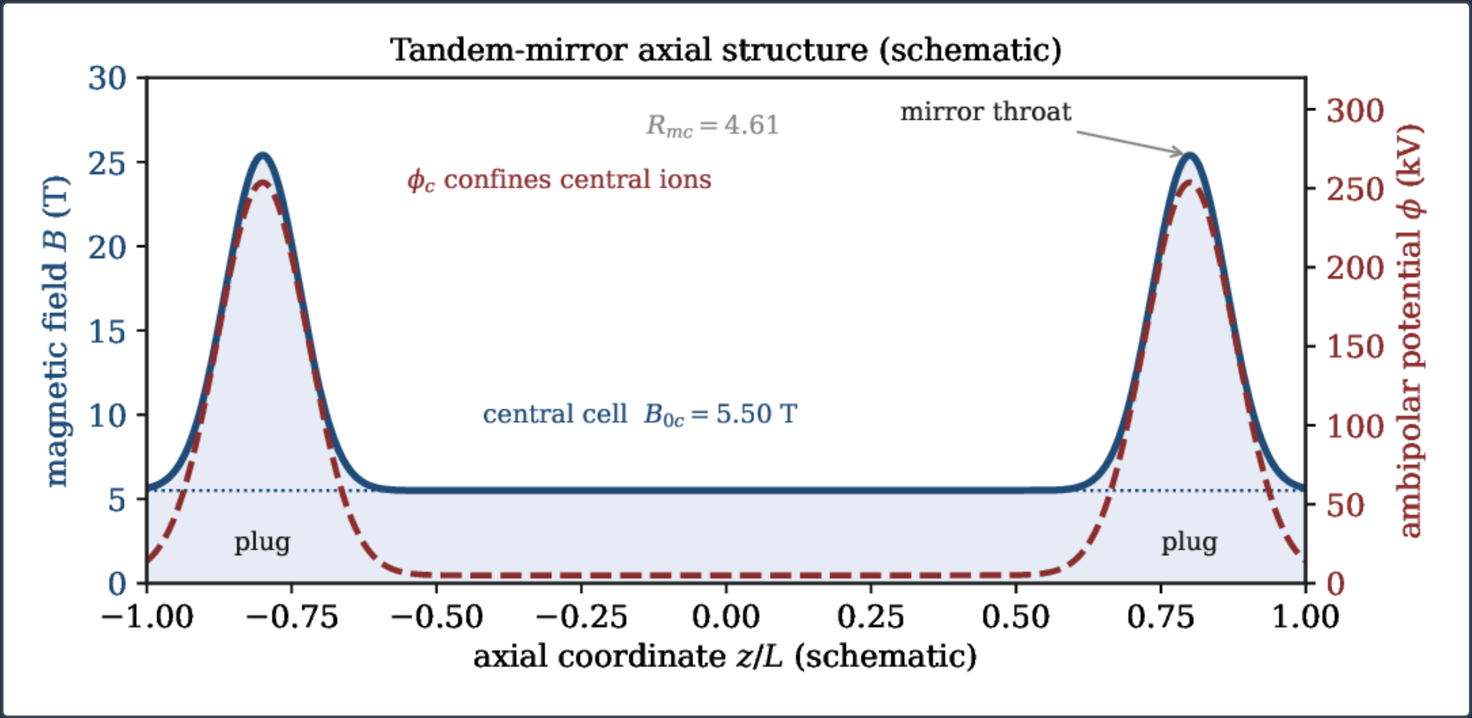

(Schematic.) Axial structure of the tandem-mirror burner: central-cell field $B_{0c} = 5.50\,\mathrm{T}$ (blue) rising to the mirror throats at $R_{mc} = 4.61$, and the ambipolar confining potential $\phi(z)$ (red, right axis) peaking at the plugs. Field and potential profiles are illustrative; the frozen scalar values (B_{0c}, R_{mc}, ϕ_c) are the design-point numbers of §2.

MHD INTERCHANGE/BALLOONING GATE

The MHD operating pressure is conservative (figure 2). At $\beta_c = 0.55$ the central cell runs a factor 1.82 below the hard $\beta = 1$ ideal limit and adjacent to the experimentally demonstrated gas-dynamic-trap value of ~ 0.6 [16,17]. On its own the central cell is interchange-unstable (equation 4) — it is long and thin, $a/\rho_i \approx 144$, so the FLR window of equation (5) is only weakly open — but the min-B anchor supplies the good-curvature line integral of equation (3) and, through the same coefficient κ_ψ, keeps the ballooning eigenvalue $\lambda_{\min} > 0$ in equation (6). The gate is thus met by an explicit stabilisation scheme with a $1.82\times$ pressure margin, not by an assumption that the pressure stays low (AG-DR-03).

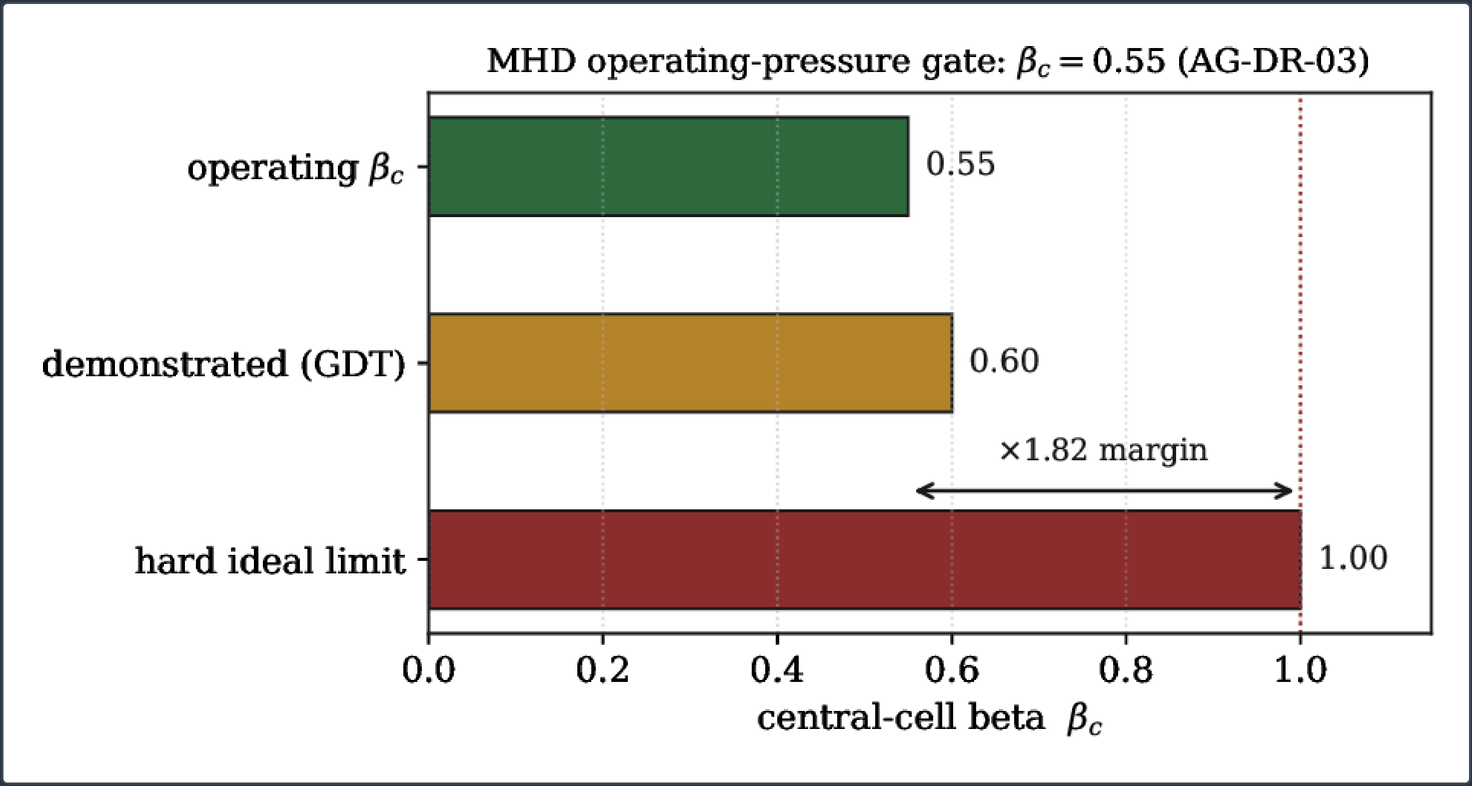

MHD operating-pressure gate. The central-cell $\beta_c = 0.55$ sits a factor 1.82 below the hard $\beta = 1$ ideal limit and next to the demonstrated gas-dynamic-trap value (~ 0.6). Data: AG-DR-03.

THE LOSS CONE AND THE WARM FILL

Figure 3 shows the velocity-space loss cone that opens at $R_{mc} = 4.61$: a half-angle $\theta_{lc} = 27.8°$ from equation (1). The warm-plasma fill of equation (8) populates the low-energy core inside the cone and flattens the perpendicular gradient that drives DCLC, while the anisotropic hot ions ($T_\perp/T_\parallel = 2.0$) that build the plug potential remain the free-energy source for the AIC branch.

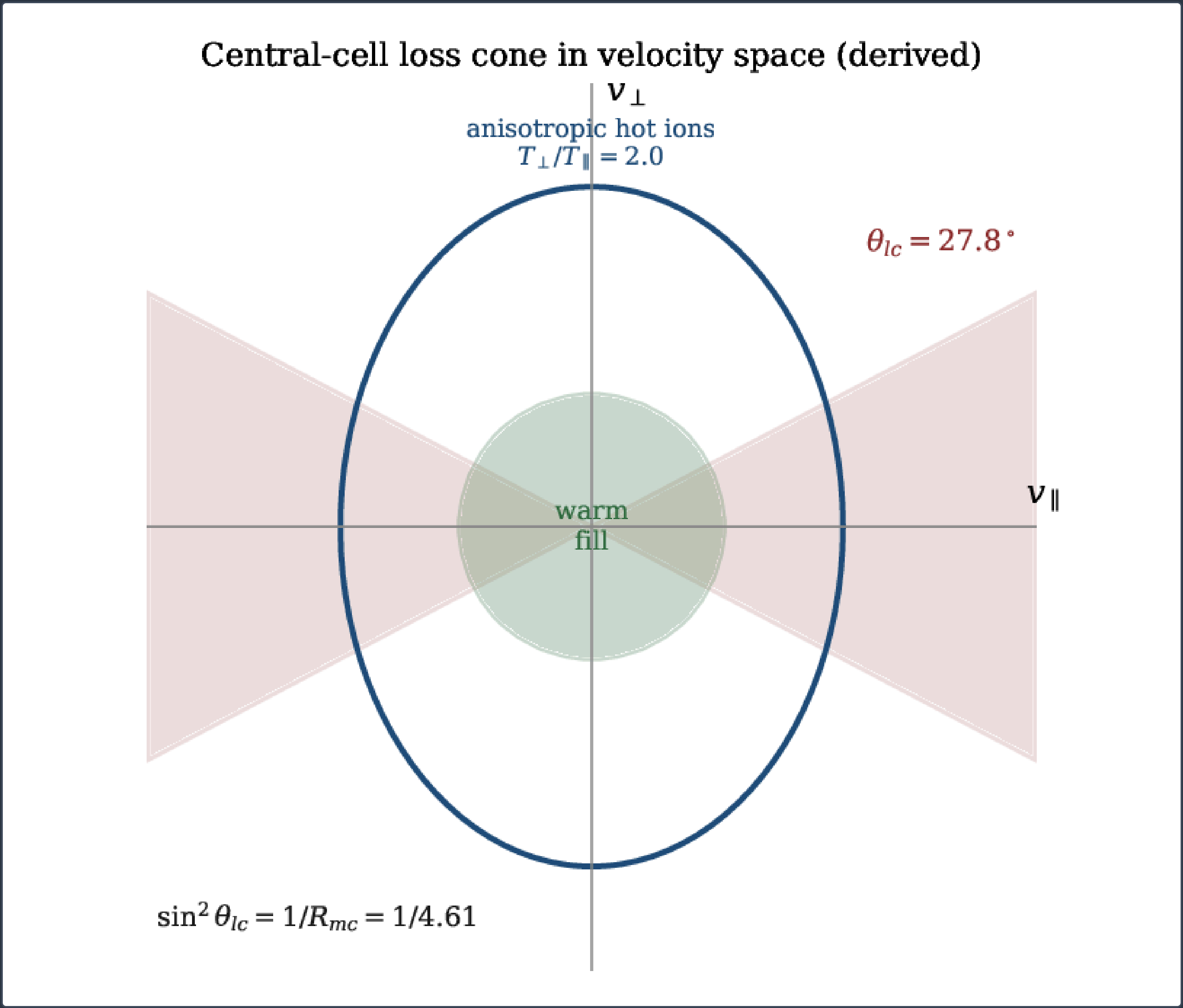

Central-cell loss cone in velocity space (derived from $R_{mc} = 4.61$ via equation 1): half-angle $\theta_{lc} = 27.8°$. The warm-fill Maxwellian (green) flattens the loss-cone gradient; the anisotropic hot population (blue) drives the AIC branch.

DCLC WARM-FILL THRESHOLD

Figure 4 reports the DCLC gate. The reduced kinetic dispersion (equation 7) gives a growth rate that falls monotonically with warm fill and crosses zero at $\sim 5.9\,\%$, reproducing the LEOPARD+WarpX PIC result of $6.25\,\% = 1/16$ within model accuracy; the two computed points bracket the crossing ($\gamma = +16.3$ at $4\,\%$, $\gamma = -0.001$ at $6.25\,\%$). This is a marginal threshold, not a comfortable margin: steeper loss-cone gradients push the required fill toward 8–$10\,\%$. Warm-ion fill is therefore a stabilisation *requirement* for the burner plug, and warm-fill provision is a design constraint rather than headroom (BU-L2-A5, HX-23).

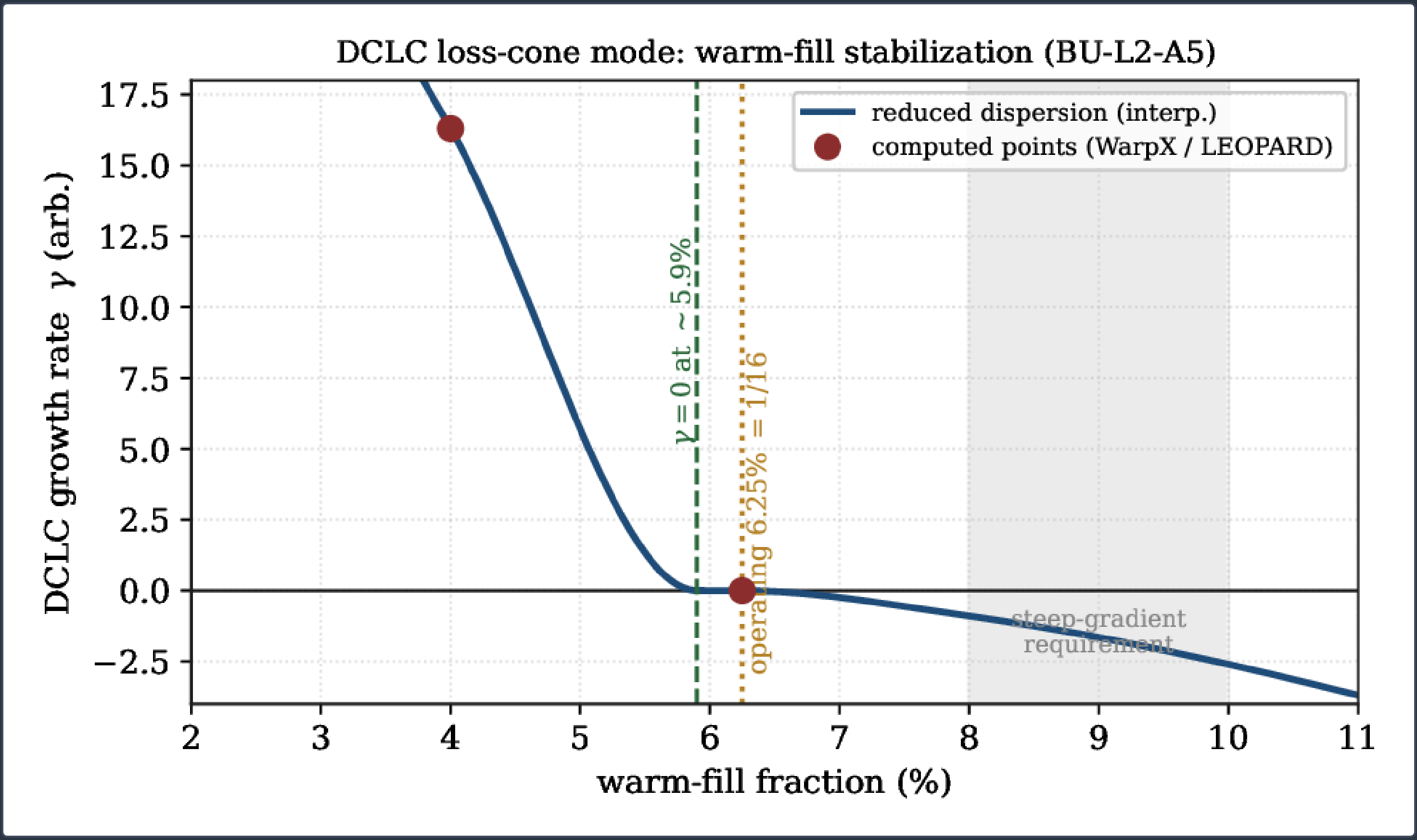

DCLC loss-cone mode. The growth rate (blue; shape-preserving interpolation of the computed points) falls monotonically with warm fill and crosses $\gamma = 0$ at $\sim 5.9\,\%$, adjacent to the $6.25\,\% = 1/16$ operating fill (gold). The shaded band marks the steeper-gradient requirement (8–$10\,\%$). Data: BU-L2-A5.

AIC GROWTH-RATE MAP

The AIC branch is not quenched by the warm fill (figure 5). Three independent 1D-hybrid PIC runs (WarpX, with Smilei cross-check) find the normalised growth rate flat at $\gamma_{\rm AIC}/\omega_{ci} \approx 0.037 \pm 0.003$ across warm-fill fractions $f_w = 0,\ 0.03,\ 0.0625,\ 0.10$ — four of four fits with $R^2 \geq 0.987$, no monotonic reduction — consistent with the anisotropy-driven scaling of equation (10) and with linear theory (0.05–$0.1\,\omega_{ci}$). AIC and DCLC share the loss-cone free-energy source but are distinct channels: warm fill closes DCLC (equation 9) but not AIC. The consequence is a bounded, fully-mapped plug-gate — modest growth, not a showstopper — whose mitigation (anisotropy/profile control) is scoped for the demonstrated-closure programme (BU-L2-A7, AG-CX-07), and which the plug-microstability controller holds inside its boundary in a PIC-in-the-loop test 10.5281/zenodo.22645811https://www.kronosfusionenergy.com/publications/a-real-time-control-suite-for-a-d-3he-tandem-mirror-bur.htmlKronos 2.76.

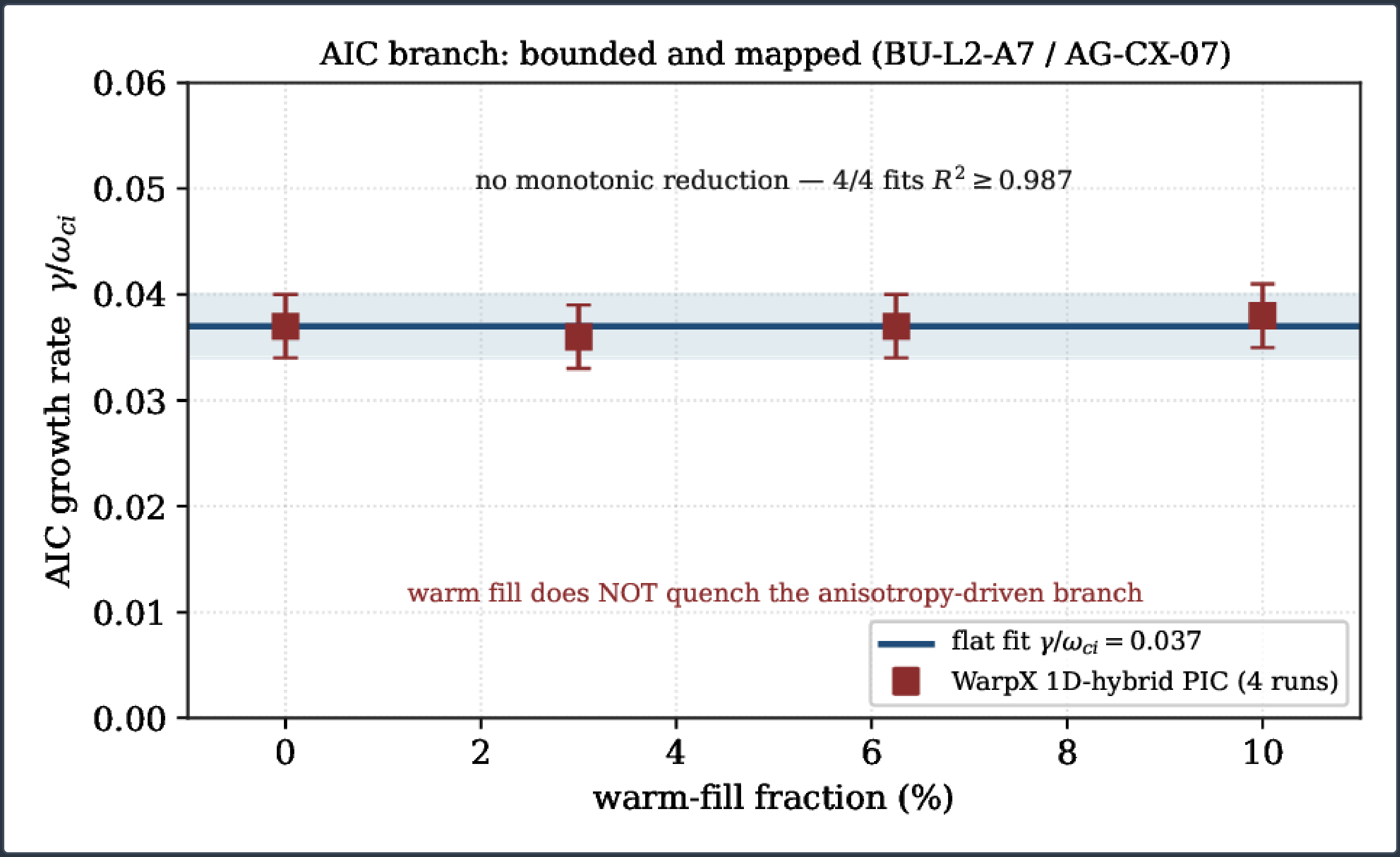

AIC branch, mapped and bounded. The normalised growth rate is flat at $\gamma/\omega_{ci} \approx 0.037 \pm 0.003$ across warm-fill fractions 0–$10\,\%$ (four PIC runs, $R^2 \geq 0.987$); warm fill does not quench the anisotropy-driven branch. Data: BU-L2-A7, AG-CX-07.

AMBIPOLAR PLUG POTENTIAL

The plug potential follows the density ratio through equation (11) (figure 6): at the design ratio $n_{\text{plug}}/n_c = 16$ the normalised potential is $e\phi_c/T_e = \ln 16 = 2.77$, which sets the Pastukhov confinement enhancement of equation (12). Holding the $16\times$ ratio is thus the physical gate on axial confinement, carried explicitly and controlled by the density-gate loop (KFE-CF-BU-019).

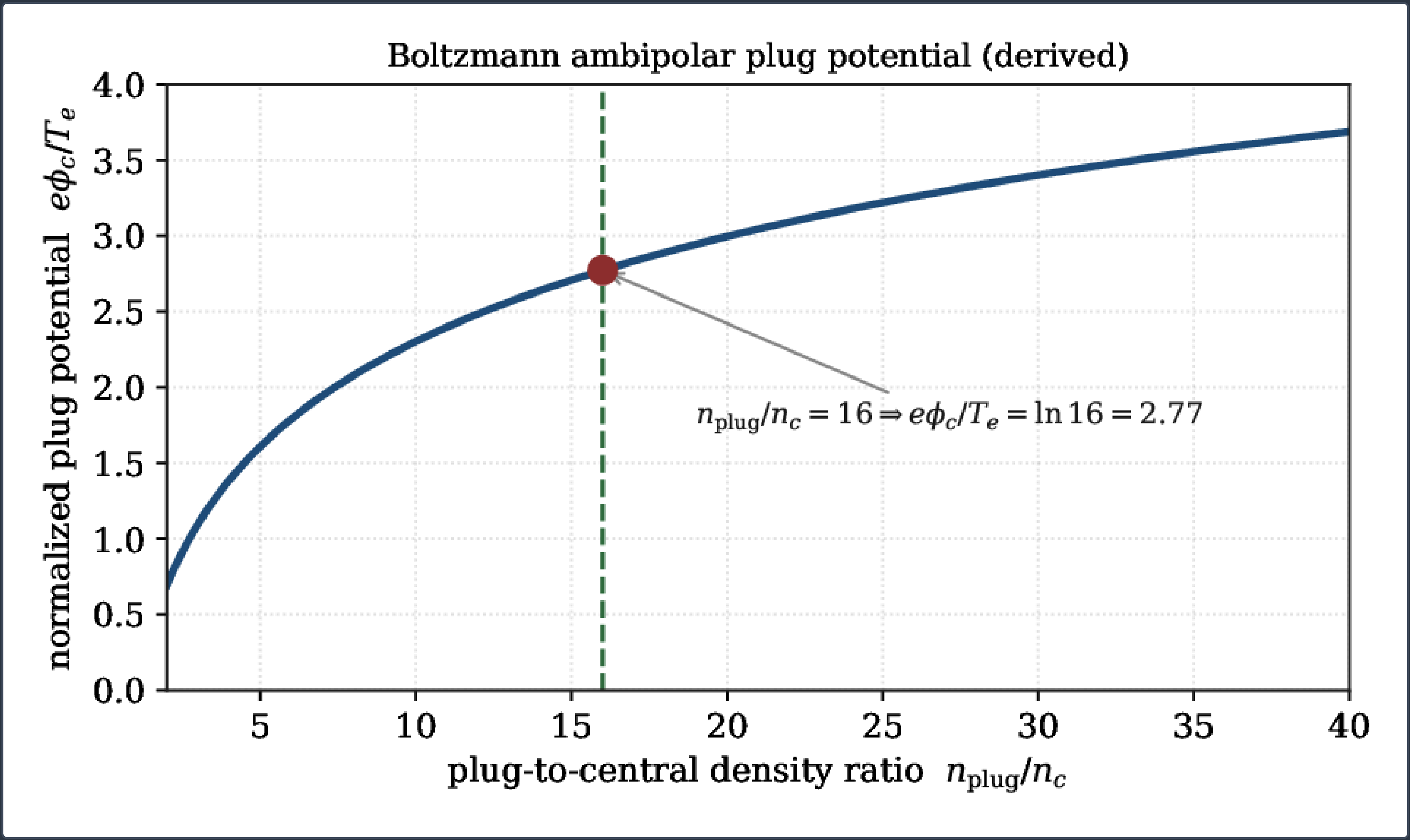

Boltzmann ambipolar plug potential $e\phi_c/T_e = \ln(n_{\text{plug}}/n_c)$ (derived, equation 11). At the design ratio 16, $e\phi_c/T_e = 2.77$.

GLOBAL ROBUSTNESS

The operating point is not fragile (figures 7–8). The 40,000-sample global UQ over $(n_e, x_{^3He}, T_i, \beta_c, B_m)$ returns $Q_E = 1.317 \pm 0.140$ with $P(Q_E > 1) = 1.000$ and zero failed evaluations (equations 16–17); the output means ($P_{\text{fus}} = 4295$ MW, $P_n = 231.6$ MW, $f_n = 5.39\,\%$, $\phi_i = 246.0$ keV) sit within a percent of the frozen design anchor ($Q_E = 1.318$, $f_n = 5.44\,\%$, $\phi_i = 248.75$ keV, $P_n = 233.95$ MW). The dominant sensitivity is to β_c (rank correlation 0.93, equation 18) — precisely the quantity the MHD stabilisation scheme of §4.2 protects, so the physics that keeps the core stable is also the physics that sets its gain. This is consistent with the cross-machine sensitivity ranking of the platform-wide UQ 10.5281/zenodo.22645893https://www.kronosfusionenergy.com/publications/global-sensitivity-and-uncertainty-quantification-acros.htmlKronos 2.88.

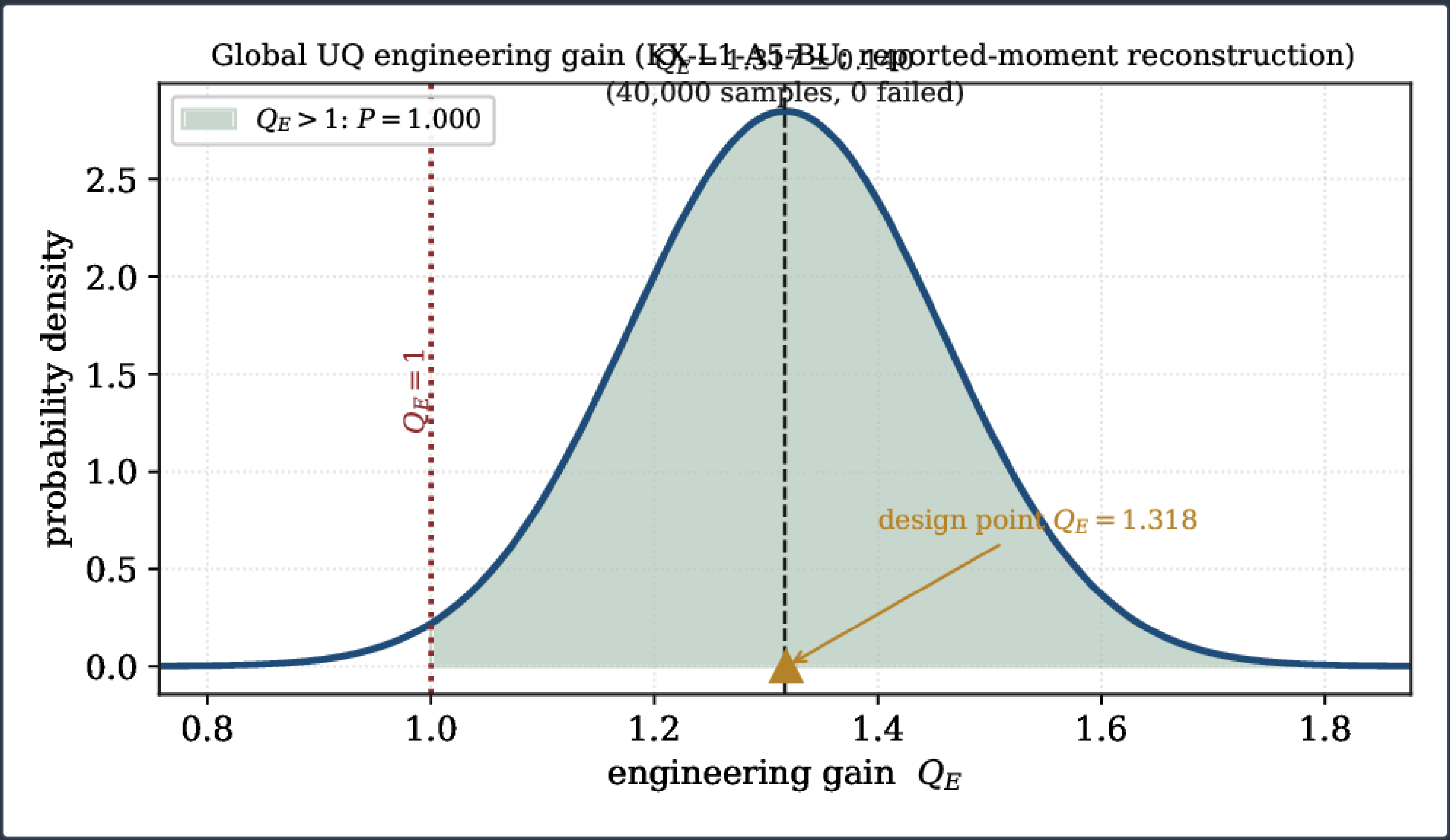

Global-UQ engineering gain (reconstructed from the reported moments $Q_E = 1.317 \pm 0.140$): the shaded tail is $P(Q_E > 1) = 1.000$ across the design ranges; the design point $Q_E = 1.318$ is marked. Data: KX-L1-A5-BU (40,000 samples, 0 failed).

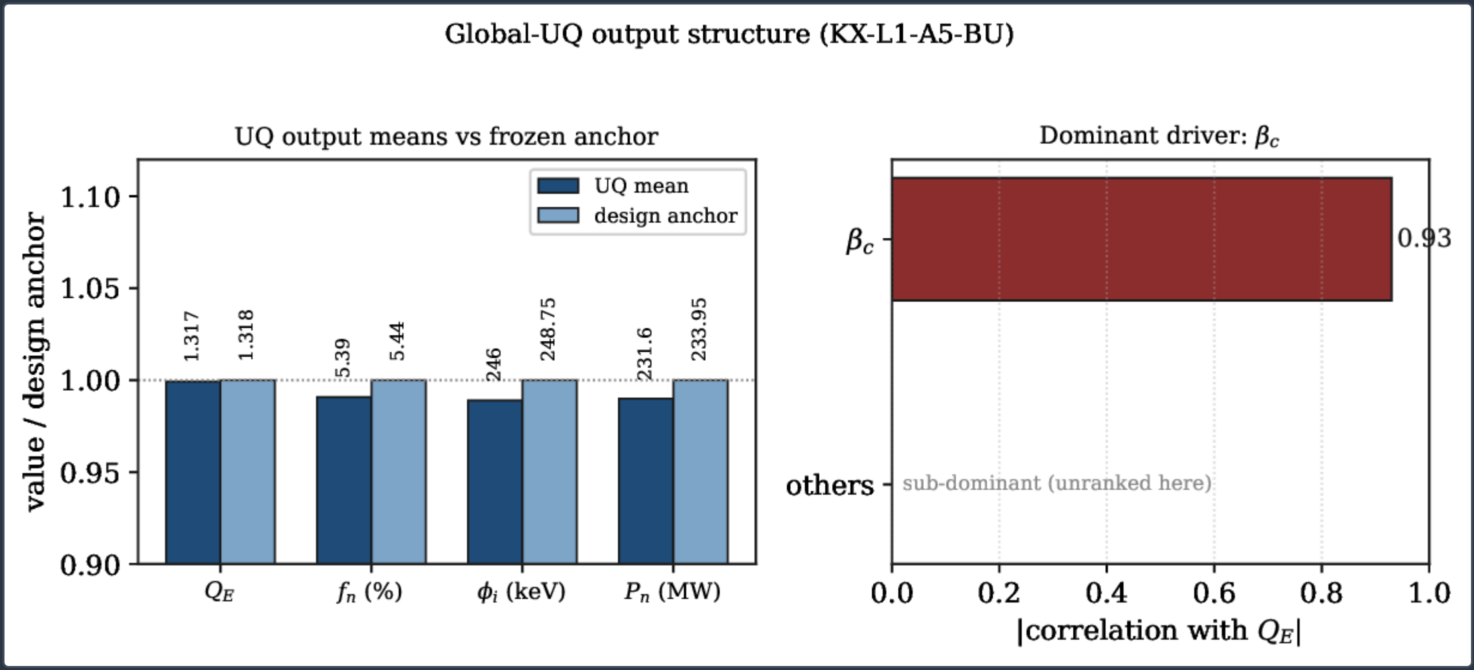

Global-UQ output structure. *Left:* UQ output means agree with the frozen design anchor to within a percent (Q_E, f_n, ϕ_i, P_n). *Right:* the dominant driver of Q_E is β_c (rank correlation **0.93**). Data: KX-L1-A5-BU.

THE SIDEWAYS-LOSS BUDGET

Figure 9 closes the loss channel deliberately held outside the UQ. Evaluating the transport closure of equations (13)–(15) at the design parameters ($T_i = 90\,$keV, $B_{0c} = 5.50\,$T, real deuteron mass) gives a thermal gyroradius $\rho_i \approx 1.11\,$cm and a Bohm diffusivity $\chi_B \approx 1.0 \times 10^3\,\mathrm{m^2s^{-1}}$, so at the design minor radius $a = 144\,\rho_i \approx 1.60\,$m the sideways confinement time is $\tau_\perp^{gB} = a^2/\chi_{gB} \sim 0.35\,$s in the gyro-Bohm estimate against $\tau_\perp^{B} \sim 2\,$ms in the Bohm estimate. The large scale separation $\rho_* = \rho_i/a \approx 1/144$ therefore places the sideways loss two orders of magnitude below the pessimistic Bohm bound, and in the gyro-Bohm regime it is subdominant to the axial channel. This is a reduced model, still being finalised against the central-cell radial-transport controller (BU-L2-A6 → KFE-CF-BU-005); the point of carrying it separately — rather than folding an assumed value into the headline gain — is what makes the $P(Q_E > 1) = 1.000$ robustness result an honest one.

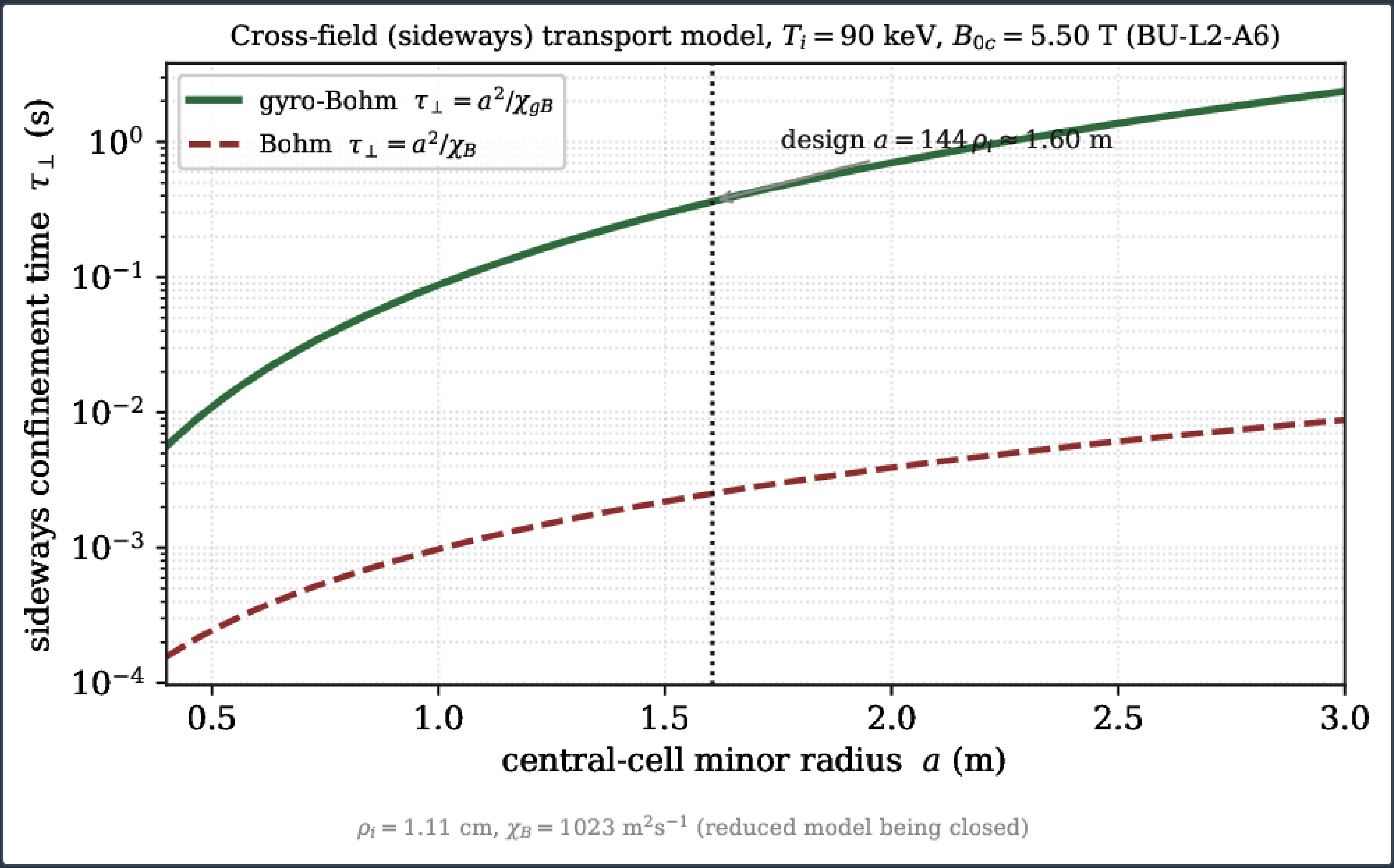

Cross-field (sideways) transport model (equations 13–15). Sideways confinement time $\tau_\perp = a^2/\chi$ versus central-cell minor radius for Bohm and gyro-Bohm diffusivities at $T_i = 90\,$keV, $B_{0c} = 5.50\,$T; the design radius $a = 144\,\rho_i \approx 1.60\,$m is marked. Reduced model being closed (BU-L2-A6).

GATE SUMMARY

Table 2 collects the central-cell gates at the frozen operating point.

GATE	VALUE	SOURCE
central-cell field B_{0c}	5.50 T	KX-L1-A18-BU
mirror-cell ratio R_{mc}	4.61	KX-L1-A18-BU
loss-cone half-angle θ_{lc}	27.8° ($\sin^2\theta_{lc} = 1/R_{mc}$)	derived
MHD operating pressure β_c	0.55 ($\times 1.82$ below $\beta = 1$)	AG-DR-03
interchange/ballooning stabilisation	min-B anchor + sloshing	AG-DR-03
DCLC warm-fill threshold	$\sim$5.9–6.25 % (= 1/16)	BU-L2-A5 / HX-23
AIC growth rate (mapped)	$\gamma/\omega_{ci} \approx 0.037 \pm 0.003$ (flat)	BU-L2-A7 / AG-CX-07
ambipolar potential	$e\phi_c/T_e = \ln 16 = 2.77$	§2.5
global-UQ engineering gain	$Q_E = 1.317 \pm 0.14$	KX-L1-A5-BU
robustness	$P(Q_E > 1) = 1.000$ (0/40,000 failed)	KX-L1-A5-BU
dominant driver	β_c (corr. 0.93)	KX-L1-A5-BU
sideways-loss budget	$\tau_\perp^{gB} \sim 0.35$ s at $a \approx 1.6$ m	BU-L2-A6

Central-cell stability, potential and robustness gates at the frozen burner operating point.

§ 5

Discussion

AGAINST THE MIRROR-PHYSICS BENCHMARKS

Each gate lands where the demonstrated mirror-physics record says it should. The MHD operating pressure $\beta_c = \mathbf{0.55}$ is below the gas-dynamic-trap value of $\sim\mathbf{0.6}$ that has been sustained MHD-stably in experiment [16,17], and a factor **1.82** below the hard ideal limit — a margin, not a frontier. The mirror-throat field ($\sim\mathbf{17}$ T) is the class demonstrated by the WHAM high-temperature-superconductor mirror [19,20], and the plug-coil peak field of **26.49** T is engineered separately with its own quench margin 10.5281/zenodo.22645915https://www.kronosfusionenergy.com/publications/engineering-the-26-49-t-plug-coil-of-a-d-he-tandem-mirr.htmlKronos 2.21. The DCLC warm-fill threshold of $\mathbf{1/16 = 6.25\,\%}$ is consistent with the long-standing result that a small warm-plasma fraction stabilises the loss-cone mode [4,7,8]; the value of our calculation is that it labels this fraction a marginal requirement rather than assuming it. The AIC growth rate $\gamma/\omega_{ci} \approx \mathbf{0.037}$ sits at the low end of the classic anisotropy-driven range [9,10], and its flatness in warm fill is the physically expected signature of an electromagnetic branch that does not draw on the loss-cone electrostatic drive.

THE SINGLE CONTROLLING KNOB

The global UQ points at β_c as the dominant driver of the engineering gain (correlation **0.93**). This is a convenient coincidence of physics and control: β_c is exactly the quantity that the interchange/ballooning stabilisation scheme of §4.2 is built to protect, and it is the natural clamp variable for a control-barrier safety layer. A core whose stability and gain are governed by one well-understood knob is easier to certify than one with many weakly-coupled sensitivities. The tandem-mirror design-space mapping study places the same operating point against WHAM and the Pastukhov-plug closure and reaches a consistent picture 10.5281/zenodo.22645911https://www.kronosfusionenergy.com/publications/tandem-mirror-design-space-mapping-for-a-d-he-burner-0-.htmlKronos 2.52.

WHAT THE SIDEWAYS-LOSS BUDGET BUYS

The gyro-Bohm/Bohm bracket of §4.8 is deliberately conservative: it does not claim a converged turbulent flux but bounds it. The two-order-of-magnitude gap between the Bohm and gyro-Bohm estimates, opened by the large scale separation $\rho_* \approx \mathbf{1/144}$, is what allows the axial power balance to stand while the radial channel is finalised. Because the long, thin geometry that weakens FLR stabilisation (equation 5) is the same geometry that makes ρ_* small, the feature that costs us in MHD buys us in transport — the anchor pays the MHD bill, the aspect ratio pays the transport one.

§ 6

Limitations

One item is carried open by design. The central-cell radial (cross-field) transport model of §2.6 is a reduced gyro-Bohm/Bohm closure, not a converged nonlinear turbulence calculation, and it is deliberately excluded from the global UQ (KX-L1-A5-BU held the plug-density ratio fixed and excluded radial transport). It is being finalised against the central-cell radial-transport controller (BU-L2-A6 → KFE-CF-BU-005), so the robustness result quoted here is the axial/stability envelope, with radial transport reported separately once the nonlinear flux converges. Stating this openly is the intended posture: the sideways channel is an explicit, separately-gated quantity, not an assumption buried in the headline number.

§ 7

Conclusion

The Kronos D–^{3}He tandem-mirror burner central cell clears its two gates that come before confinement, at the frozen operating point. In MHD, $\beta_c = 0.55$ runs a factor 1.82 below the hard $\beta = 1$ limit and is held against interchange and ballooning by a min-B anchor and sloshing-ion stabilisation, the same anchored good-curvature term entering both the flute integral (equation 3) and the ballooning eigenproblem (equation 6). In velocity space, the DCLC loss-cone mode is quenched above a monotone warm-fill threshold of ~ 5.9–$6.25\,\%$ ($= 1/16$), and the anisotropy-driven AIC branch is mapped flat at $\gamma/\omega_{ci} \approx 0.037 \pm 0.003$ across 0–$10\,\%$ warm fill — a bounded, characterised plug-gate rather than a surprise. A $40{,}000$-sample global UQ returns $Q_E = 1.317 \pm 0.14$ with $P(Q_E > 1) = 1.000$ and zero failed evaluations, dominated by β_c — the quantity the stabilisation scheme protects. The one loss channel held outside that envelope, central-cell cross-field transport, is carried as an explicit, gyro-Bohm-bounded item. The core is MHD- and microstability-sound, with a quantified margin and an honest, separately-closed sideways-loss budget.

Part of the Kronos Fusion Energy 2026 design series. We thank the de-risking campaign team for the independent re-runs recorded in the Physics De-Risking Register, and the open-source plasma-physics community whose codes (WarpX, Smilei, LEOPARD, CQL3D, CGYRO) made these calculations possible.

Reproducibility. The stability, potential and robustness values reported here are frozen results (AG-DR-03, BU-L2-A5, BU-L2-A7, AG-CX-07, KX-L1-A5-BU, KX-L1-A18-BU, HX-23) in the Kronos Physics De-Risking Register, doi:10.5281/zenodo.22133057. This paper is archived at doi:10.5281/zenodo.22645854; official version: https://www.kronosfusionenergy.com/publications/central-cell-radial-transport-and-interchange-balloonin.html and its official version is hosted at https://www.kronosfusionenergy.com/publications/central-cell-radial-transport-and-interchange-balloonin.html. The figure-generation script (`make_figs_centralcell_258.py`), which reads only the frozen scalar results above, is archived with the deposit; all runs are seed-deterministic (seed 20260726).

Data availability tocsectionData availability This paper is archived at doi:10.5281/zenodo.22645854. The PIC, kinetic-dispersion and Monte-Carlo UQ inputs and the figure scripts are archived with the deposit and reference the Kronos 2026 series and its Physics De-Risking Register (doi:10.5281/zenodo.22133057). Any economic analysis is reported separately and is not included in the public deposit.

Competing interests tocsectionCompeting interests Provisional patent applications relating to aspects of this work have been filed. The authors declare no other competing interests.

APPARATUS

Portfolio, People & Record

The intellectual-property estate, the people who built it, the limitations that gate it, and the sources it rests on.

1	4	40	27
GRANTED PATENT	2026 PROVISIONALS	TEAM MEMBERS	2022 PROVISIONALS

INTELLECTUAL PROPERTY

The patent portfolio

The estate spans a granted high-field magnet patent, pending utility and 2026 provisional filings that map to the two products, a digital-twin control provisional, a registered trademark application, and the original 2022 provisional family. Every patentable disclosure in the five-paper arXiv drop was protected **before** publication: the breeder and burner provisionals were filed 1–2 August, and a publication-gap omnibus filing the evening before the drop swept up the DEC, plasma-control, and REBCO-winding matter of the three otherwise-unprotected papers. Patent numbers and application serials are matters of public record; claim scope is summarised, not reproduced.

GRANTED & PENDING UTILITY

US 12,009,112	High-field tilted graded-REBCO magnet architecture (KRONO-002A) · *app. 17/878,550*	GRANTED
US 17/878,507	Core device / method (KRONO-001A) · *utility*	PENDING

2026 PROVISIONAL FILINGS — MAPPED TO THE PRODUCTS

64/124,209	Hyperion — spherical-tokamak tritium / helium-3 foundry · *breeder · filed Aug 2026*	FILED
64/124,220	Aegis / MetroVolt — synchrotron-cutoff, fuel-selection & plug-winding · *generator · filed Aug 2026*	FILED
64/115,167	KRONOS-CTRL digital-twin plant control · *provisional · filed Jul 2026*	FILED
64/005,440	Integrated spherical-tokamak fusion architecture · *early integrated-architecture filing · filed Mar 2026*	FILED
64/105,530	Negative-triangularity spherical-tokamak architecture · *foundational ST filing · filed Jul 2026*	FILED
64/128,097	Publication-gap omnibus — quasineutral two-species expander DEC · provenance-gated / latency-split plasma control · as-built high-field winding & conductor architecture · *filed 7 Aug 2026, the evening before the arXiv drop*	FILED

TRADEMARK & ORIGIN

FTK-98801894	Kronos Fusion Energy — trademark application	FILED
KR-2022-*	Original provisional family (KR-2022-00001 … 00027) · *27 filings, 2022*	PRIORITY

The narrow, defensible magnet novelty — the specific conductor and the digital-twin winding optimisation, not high-field REBCO as a category — is the commercial core that can earn ahead of any Q > 1 milestone, with markets in fusion magnet supply, MRI/NMR, accelerators, and proton therapy. The claim is scoped honestly: the high field is a *system field* result, not a stand-alone-coil record; the small-bore plug coil is structurally infeasible as a bare winding but resolved by a stress-managed structural shield (feasible-pending-FEA); and the winding-tape experiment returned a *null result*. The value is the method, not a field record.

THE TEAM

Founding partners, board, advisors & auditors

Kronos is built by a bench of advanced-fuel-fusion, high-field-magnet, direct-conversion, and materials specialists, with a board and operations team drawn from defense, national laboratories, and industry. Dates are shown as ranges; where a tenure has ended or is term-ending, the range says so.

FOUNDING PARTNERS — SCIENCE

Dr. Gerald Kulcinski
Co-Founder · Helium-3 & Advanced-Fuel Fusion
UW–Madison · 2023–Present

Dr. Carl Weggel
Chief Scientist / S.M.A.R.T. Design
MIT Alcator Program · 2022–Present

Dr. Robert J. Weggel
Magnetic Field Design
MIT Magnet Lab · 2022–Present

BOARD

Priyanca Ford
Founder & CEO · Executive Board
2022–Present

Bandel Carano
Finance / Strategy
Oak Investment Partners / Stanford · 2025–2026

Patrick Schweiger
Fusion Device Engineering
Oklo / CFS / TerraPower · 2025–Present

SCIENTIFIC ADVISORS

Dr. Steven O. Dean
Fusion Policy & History
DOE / Fusion Power Associates · 2025–Present

Dr. Patrick H. Diamond
Plasma Turbulence & Transport
UC San Diego · 2025–Present

Dr. Jack J. Dongarra
HPC & Numerical Algorithms
Turing Award · 2025–Present

Dr. Nasr M. Ghoniem
Chief Material Scientist
UCLA · 2025–Present

Dr. Siegfried Glenzer
Plasma Physics & Laser Fusion
Stanford / SLAC · 2022–Present

Dr. David A. Hammer
Pulsed-Power Fusion
Cornell · 2025–Present

Dr. Donald A. Spong
Plasma Theory & Confinement
ORNL · 2025–Present

Dr. Curtis Smith
Risk Assessment & Nuclear PRA
MIT / Idaho National Lab · 2025–Present

RADM (Ret.) David Goggins
Naval Engineering & Power-Plant Design
U.S. Navy · 2023–2026

Dr. Konstantin Batygin
Mathematician
Caltech · 2022–2025

Dr. Ruben Fair
Magnet Design / ITER Liaison
PPPL / Jefferson Lab · 2022–2025

Dr. Paul S. Weiss
Materials & Nanotechnology
UCLA · 2022–2025

SCIENTIFIC AUDITORS

Dr. Wilfred A. Cooper
Plasma Equilibrium Theory
EPFL / Swiss Plasma Center · 2025–Present

Dr. Ahmed Hassanein
Plasma–Material Interactions
Purdue / Argonne · 2025–Present

Dr. Patrick E. Hopkins
Extreme Thermal Materials
U. of Virginia · 2025–Present

Dr. Peter Hosemann
Materials Joining & Structural Integrity
UC Berkeley · 2025–Present

Dr. Travis W. Knight
Advanced Nuclear Fuels & Systems
U. of South Carolina · 2025–Present

Dr. Philippe Lebrun
Cryogenics & Magnet Cooling
CERN · 2025–Present

Dr. Nitendra Singh
Nuclear Safety & Fuel Cycle
ITER · 2025–Present

Dr. Guido Van Oost
Magnetic Confinement & Fusion Systems
Ghent University · 2025–Present

Dr. Gary S. Was
Radiation Materials & Structural Integrity
U. of Michigan · 2025–Present

Dr. Ray Sedwick
Direct Energy Conversion
U. of Maryland · 2025

OPERATIONS

Michael Laughlin
Chief Operating Officer
2022–Present

Martin Owens
Chief Strategy Officer
LANL / GE Hitachi · 2022–Present

MG (Ret.) Paul Pardew
Chief Contracting Officer
Army Contracting Command · 2022–Present

David Beck
Fusion Commercialization
U.S. Space Force · 2024–Present

Sushma Bhatia
Environmental & Legislative
Google · 2022–Present

Michael De Frenza
Technology Licensing
2023–Present

MG (Ret.) Robin L. Fontes
Cybersecurity & Defense
Army Cyber Command · 2022–Present

Vijay Gehani
Supply Chain & Components
INOX India · 2024–Present

Jon Michel Greenwood
IT & AI Infrastructure
Live Nation · 2023–Present

Brian C. O'Neill
National Security
CIA / ODNI · 2022–Present

Gen. (Ret.) Gustave F. Perna
DoD Liaison
Operation Warp Speed · 2022–2023

Andrea Romero
Marketing Lead
2022–Present

Legal counsel is retained; those roles are held on the internal roster and are not listed here.

SOURCES

References

1 G I Dimov, V V Zakaidakov and M E Kishinevskii, *Thermonuclear confinement with twin mirror systems*, Sov. J. Plasma Phys. **2** (1976) 326.

2 T K Fowler and B G Logan, *The tandem mirror reactor*, Comments Plasma Phys. Control. Fusion **2** (1977) 167.

3 R F Post, *The magnetic mirror approach to fusion*, Nucl. Fusion **27** (1987) 1579. doi:10.1088/0029-5515/27/10/001

4 M N Rosenbluth and R F Post, *High-frequency electrostatic plasma instability inherent to "loss-cone" particle distributions*, Phys. Fluids **8** (1965) 547.

5 B B Kadomtsev, *Hydromagnetic stability of a plasma*, in *Reviews of Plasma Physics*, Vol. 2 (Consultants Bureau, New York, 1966) p. 153.

6 J P Freidberg, *Ideal MHD* (Cambridge University Press, 2014).

7 R F Post and M N Rosenbluth, *Electrostatic instabilities in finite mirror-confined plasmas*, Phys. Fluids **9** (1966) 730.

8 D E Baldwin, *End-loss processes from a mirror machine*, Rev. Mod. Phys. **49** (1977) 317. doi:10.1103/RevModPhys.49.317

9 R C Davidson and J M Ogden, *Electromagnetic ion cyclotron instability driven by ion energy anisotropy in high-beta plasmas*, Phys. Fluids **18** (1975) 1045.

10 S P Gary, *Theory of Space Plasma Microinstabilities* (Cambridge University Press, 1993).

11 J Kesner, *Interchange stability of a tandem-mirror central cell*, Nucl. Fusion **20** (1980) 557.

12 D E Baldwin and B G Logan, *Improved tandem mirror fusion reactor*, Phys. Rev. Lett. **43** (1979) 1318.

13 W M Tang, L D Pearlstein and H L Berk, *Finite-Larmor-radius stabilization of the interchange mode*, Phys. Fluids **15** (1972) 1153.

14 A D Beklemishev, P A Bagryansky, M S Chaschin and E I Soldatkina, *Vortex confinement of plasmas in symmetric mirror traps*, Fusion Sci. Technol. **57** (2010) 351.

15 D D Ryutov, *Open-ended traps*, Sov. Phys. Usp. **31** (1988) 300.

16 A A Ivanov and V V Prikhodko, *Gas dynamic trap: experimental results and future prospects*, Phys. Usp. **60** (2017) 509.

17 P A Bagryansky *et al.*, *Threefold increase of the bulk electron temperature of plasma discharges in a magnetic mirror device*, Phys. Rev. Lett. **114** (2015) 205001.

18 V P Nagornyj, D D Ryutov and G V Stupakov, *Flute instability of plasma in a gas-dynamic trap*, Nucl. Fusion **24** (1984) 1421.

19 D Endrizzi *et al.*, *Physics basis for the Wisconsin HTS Axisymmetric Mirror*, J. Plasma Phys. **89** (2023) 975890501.

20 T K Fowler, R W Moir and T C Simonen, *A new simpler path to fusion energy*, Nucl. Fusion **57** (2017) 056014. doi:10.1088/1741-4326/aa5e54

21 V P Pastukhov, *Collisional losses of electrons from an adiabatic trap in a plasma with a positive potential*, Nucl. Fusion **14** (1974) 3. doi:10.1088/0029-5515/14/1/001

22 R H Cohen, M E Rensink, T A Cutler and A A Mirin, *Collisional loss of electrostatically confined species in a magnetic mirror*, Nucl. Fusion **18** (1978) 1229.

23 J Candy, E A Belli and R V Bravenec, *A high-accuracy Eulerian gyrokinetic solver for collisional plasmas*, J. Comput. Phys. **324** (2016) 73. doi:10.1016/j.jcp.2016.07.039

24 L Fedeli *et al.*, *Pushing the frontier in the design of laser-based electron accelerators with groundbreaking mesh-refined particle-in-cell simulations on exascale-class supercomputers*, Proc. Int. Conf. for High Performance Computing (SC22), 2022.

25 J Derouillat *et al.*, *Smilei: a collaborative, open-source, multi-purpose particle-in-cell code for plasma simulation*, Comput. Phys. Commun. **222** (2018) 351. doi:10.1016/j.cpc.2017.09.024

26 P Astfalk and F Jenko, *LEOPARD: a grid-based dispersion relation solver for arbitrary gyrotropic distributions*, J. Geophys. Res. Space Physics **122** (2017) 89.

27 R W Harvey and M G McCoy, *The CQL3D Fokker–Planck code*, Proc. IAEA Technical Committee Meeting on Advances in Simulation and Modeling of Thermonuclear Plasmas (Montreal, 1992) p. 489.

28 I M Sobol, *Global sensitivity indices for nonlinear mathematical models and their Monte Carlo estimates*, Math. Comput. Simul. **55** (2001) 271. doi:10.1016/S0378-4754(00)00270-6

29 G L Kulcinski and J F Santarius, *Advanced fuels under debate*, Nature **396** (1998) 724.

30 W M Nevins, *A review of confinement requirements for advanced fuels*, J. Fusion Energy **17** (1998) 25.

31 B N Sorbom *et al.*, *ARC: a compact, high-field, fusion nuclear science facility and demonstration power plant with demountable magnets*, Fusion Eng. Des. **100** (2015) 378. doi:10.1016/j.fusengdes.2015.07.008

32 P I Ford, *Kronos Physics De-Risking Register*, Kronos Fusion Energy 2026 series. doi:10.5281/zenodo.22133057

COLOPHON

How this document was made

The Kronos Fleet — Combined Editorial, 2026 is set in **Fraunces** (display), **Gelasio** (text), and **IBM Plex Mono** (data & equations), carried forward from the Kronos editorial design system.

The figures are rendered at 300 dpi from the deposited generator scripts; the document is composed as a single self-contained file with embedded fonts and imagery, paginated to US Letter, and rendered to PDF through a headless Chromium engine in matched light and dark editions.

Every headline quantity carries an evidence class; withdrawn and restated values are marked as such. Nothing herein is frozen beyond the founder-approved Tier-A set.

Explore it live — turn the interactive 3-D model, run the deposited solvers in the physics validator, and watch the companion film series.

LEGAL NOTICE

Notice, status, and distribution

Conceptual design & simulation study. This document reports a conceptual design and simulation study. It is not a construction commitment, a safety-analysis report, a regulatory filing, or an offer of securities. Forward-looking statements — schedules, costs, market sizes, and performance — are estimates subject to the limitations set out in the Simulations part and may change.

Numbers and their classes. Quantities are reported with evidence classes and case labels; modelled, assumed, and requirement-class values are identified as such and are not to be quoted without their labels.

Public edition. This edition carries the physics and design only; all financial, funding, and defense-commercial content has been removed for public distribution. The scientific text corresponds to the arXiv and journal submissions.

THE 2026 KRONOS SERIES

One programme, many papers

This editorial is one paper in the Kronos 2026 series — a real fusion company's complete, reproducible physics record for a spherical-tokamak breeder and its low-neutron D–^{3}He tandem-mirror burners. Every headline number is a frozen anchor in the Physics De-Risking Register.

Explore the whole programme: the De-Risking Register, the interactive 3-D model, and the physics validator.

KRONOS FUSION ENERGY

Central-Cell Radial Transport and Interchange/Ballooning MHD Stability in a D-3He Tandem-Mirror Burner: The Sideways-Loss and Stability Gates

A real fusion company building real machines. Explore the science, live.

Zenodo · doi:10.5281/zenodo.22645854

Read on kronosfusionenergy.com

The Physics De-Risking Register